JOURNAL OF MODERN OPTICS, 1999, VOL. 46, NO. 2, 303–326

Three-dimensional dynamic light scattering

EKKEHARD OVERBECK and CHRISTIAN SINN†
Institut für Physik der Johannes-Gutenberg-Universität,
Staudingerweg 7, 55099 Mainz, Germany

(*Received 12 May 1998*)

Abstract. We describe the employment of a novel light-scattering scheme for the decorrelation of multiple scattering in strongly turbid samples. The three-dimensional scheme, which has been proposed already theoretically, shows certain advantages compared with the two-colour apparatus, which is commercially available. We describe our set-up in detail; features are the use of modern semiconductor laser diodes and contemporary single-mode fibre receivers. We show experimentally that the optimal signal-to-noise ratio (or intercept) $\beta_{opt} = 0.20$, which is obtainable with our set-up, can be quantitatively calculated from the measured uncertainties in the alignment. In particular, we give a detailed derivation of all factors influencing the signal-to-noise ratio. We investigate a highly turbid polystyrene latex sample with a nominal radius of 57.5 nm and 5% solid content, to demonstrate clearly measurements of the cross correlation function without distortions due to multiple scattering. With its turbidity of 3 mm^{-1} at 790 nm this represents the most turbid sample which has been investigated by dynamic light scattering to date.

Downloaded By: [Carl Zeiss AG] At: 12:49 11 November 2009

1. Introduction

For about 25 years, dynamic light scattering has been used as a powerful tool for the investigation of temporal fluctuations in low-turbidity media [1]. The principle of this technique is quite simple: a plane light wave (in practice usually a laser beam) with wave-vector $\mathbf{k}_i$ is directed onto the sample under investigation. If the sample is spatially inhomogeneous, a scattered spherical wave emerges with wave-vector $\mathbf{k}_f$ under a difference (scattering) vector $\mathbf{q} = \mathbf{k}_i - \mathbf{k}_f$, thus defining the scattering plane (figure 1(*a*)). As the characteristic frequency of the temporal fluctuations is small compared with the frequency of light, its wavelength λ remains essentially unchanged upon scattering, which leads to $q = (4\pi n/\lambda) \sin(\theta/2)$; n is the refractive index of the medium and θ the scattering angle.

The information of the temporal fluctuations is retrieved by constructing a correlation function of the scattered light intensity of a given Fourier component according to

$$G_{11}^{I}(\mathbf{q}, \tau) = \lim_{T\to\infty}\left(\frac{1}{T}\int_{t=t_0}^{t_0+T} I_1(\mathbf{q}, t) I_1(\mathbf{q}, t+\tau)\,\mathrm{d}t \equiv \langle I_1(\mathbf{q}, t_0)\cdot I_1(\mathbf{q}, t_0+\tau)\rangle\right). \quad (1)$$

For equilibrium systems $G_{11}^{I}(\mathbf{q}, \tau)$ does not depend on t_0, which henceforth is chosen to be $t_0 = 0$. $G_{11}^{I}(\mathbf{q}, \tau)$ is an (intensity) autocorrelation function in the sense

† Author for correspondence. http://www.uni-mainz.de/FB/Physik/Kolloide.

0950–0340/99 $12·00 © 1999 Taylor & Francis Ltd.

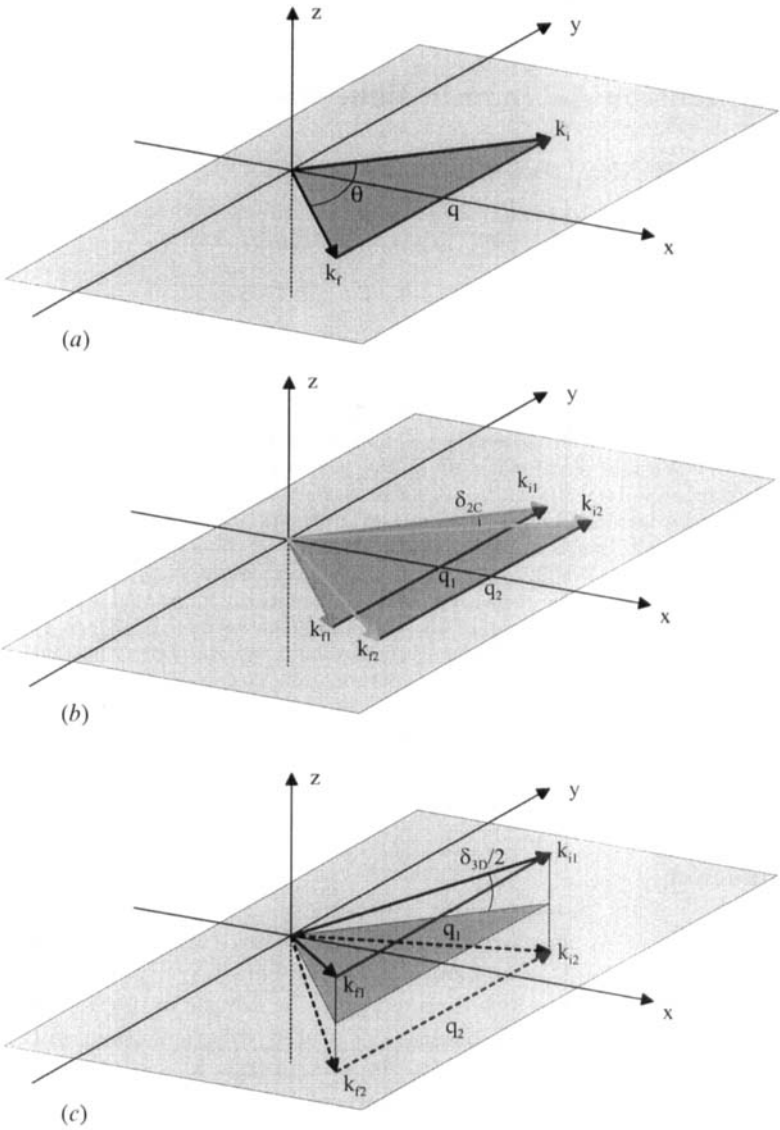

Figure 1. Evolution of dynamic light scattering: (*a*) conventional autocorrelation scheme; (*b*) two-colour cross correlation scheme; (*c*) three-dimensional cross correlation scheme.

that the measured intensity from a single detector is correlated at different times; this is denoted by the subscript 11.

If the probability of scattering events increases, scattered light will be detected which has lost its close relation to the scattering vector given by the geometrically defined initial and final wave-vectors respectively. Imagine, as an example, the dominant double scattering, where two subsequent scattering events take place in the scattering plane. Then there exists an intermediate scattering vector, which leads to two Fourier components, which are in general different, that is singly and doubly scattered light; these are detected at the same scattering angle. This significantly complicates the evaluation of the intensity autocorrelation function.

Downloaded By: [Carl Zeiss AG] At: 12:49 11 November 2009

In order to deal with this problem, some 10 years ago Phillies proposed to construct a cross correlation function according to

$$G_{12}^{I}(\mathbf{q}, \tau) \equiv \langle I_1(\mathbf{q}, 0) I_2(\mathbf{q}, \tau) \rangle, \tag{2}$$

where two opposing laser beams with the same wavelength cross the sample, while the scattered light is detected by two different detectors under an angle of 90°; this is denoted by the subscript 12. Phillies showed both theoretically [2] and experimentally [3] that $G_{12}^{I}(\mathbf{q}, \tau)$ contains the same physical information as $G_{11}^{I}(\mathbf{q}, \tau)$. However, $G_{12}^{I}(\mathbf{q}, \tau)$ is essentially free from multiple-scattering contributions, as they are decorrelated and contribute to the baseline only.

Meanwhile, different approaches have been published in order to measure the q-dependent dynamics of turbid samples without distortions due to multiple scattering. In this contribution, we shall describe the experimental realization of a light scattering cross correlation scheme, which was first proposed by Schätzel [4], namely the three-dimensional cross correlation experiment. One particular goal of our experiment is to approach the limits of multiple-scattering decorrelation, that is to extend the application of cross correlation experiments to as highly turbid samples as possible.

Clearly, the dynamics of strongly turbid samples can be investigated utilizing the photon diffusion approach [5], which inherently relies on the assumption that *no* singly scattered light reaches the detector. This implies that the spatial scale accessible by dynamic light scattering via $\mathbf{q}$ is lost. Accordingly, with our experiment we rely on the fact that singly scattered light is present to an extent which enables us to determine the cross correlation function with a sufficient signal-to-noise ratio β. In fact we are able to include a complete theoretical discussion of β and its comparison with experimentally determined values, which gives quantitative agreement.

The paper is organized as follows. We shall first give a historical overview of cross correlation experiments in section 2. We then shall review some aspects of cross correlation experiments in general (section 3), before we describe our novel apparatus together with some experimental details and results (section 4). Our set-up is thought to be an improving development of the two-colour experiment, which has been described in detail in a previous issue of this journal [6].

2. State of the art in cross correlation experiments

The idea of exploiting a cross correlation experiment is quite old. The first experiments were performed in order to suppress unwanted detector nonlinearities by splitting the scattered light path and cross correlating the fluctuations using two detectors [7, 8]. This method, currently called quasi-cross correlation, enables the use of time lags τ otherwise affected by dead time or after-pulsing of the detectors. The main underlying assumption is the statistical independence of the nonlinear effects in both detectors.

Multiple-scattering decorrelation is quite similar in the sense that scattering experiments with different scattering vectors $\mathbf{q}$ are statistically independent. If two independent light-scattering experiments with different $\mathbf{k}_i$ are performed on the same scattering volume, only light scattered by the same scattering centres gives rise to a correlated contribution, where in addition the intermediate scattering vectors have to be the same for both experiments. This condition can only be

Downloaded By: [Carl Zeiss AG] At: 12:49 11 November 2009

fulfilled by singly scattered light, which means that multiply scattered light is decorrelated effectively. The requirement for a working cross correlation experiment is that the scattering vectors of both experiments have to be equal in magnitude and, in addition, either parallel or antiparallel. This can be cast into the condition $|\mathbf{q}_1 \cdot \mathbf{q}_2| = |\mathbf{q}_1| \cdot |\mathbf{q}_2|$, which both experiments employing different $\mathbf{k}_i$ have to fulfil.

As previously mentioned, the first experimental approach making use of this recipe was by Phillies [3], who already pointed out that a generalization of his set-up to two wavelengths would enable the method to be extended to different scattering angles.

A corresponding set-up was proposed by Dhont and de Kruif [9], which unfortunately failed to achieve the same direction of the scattering vector in both experiments. This becomes obvious if their figure 4 is compared with figure 1 in the paper by Segrè *et al.* [6]. Consequently, in a subsequent experimental paper, Mos *et al.* [10] utilized the Phillies arrangement to demonstrate impressively the merits of the cross correlation technique.

Downloaded By: [Carl Zeiss AG] At: 12:49 11 November 2009

In 1988, Drewel *et al.* [11] demonstrated in the laboratory of Schätzel in Kiel a working dual-colour cross correlation experiment, a scheme of which is shown in figure 1(*b*). They used the two main lines of an Ar^+ gas laser ($\lambda_1 = 514.5\,\text{nm}$; $\lambda_2 = 488.0\,\text{nm}$) running in multiline operation, which were separated by a specially manufactured Köster prism employing a dichroic layer. The parallel beams of different colours were directed into the sample cell with the same difference angle by a single transmission lens. A similar lens on the detection side picks up the scattered light which is split by a beam splitter and colour separated by narrow-bandwidth filters in front of the detectors. For the first time they report a credible value for a cross correlation signal-to-noise ratio, which they determined to be $\beta > 0.6$.

This set-up used by Drewel *et al.* was redesigned by W. Peters in order to allow a simpler alignment and to avoid those problems encountered with the dichroic layer of the Köster prism. This set-up is commercially available; its features, together with interesting applications, have been demonstrated by Segrè *et al.* [6]. In particular, an unexpected and up-to-date unexplained relation between the diffusional and the rheological properties of concentrated hard-sphere suspensions was observed [12].

In a theoretical paper [4], Schätzel suggested using a three-dimensional cross correlation experiment, the scheme of which is shown in figure 1(*c*). As both individual scattering experiments share a common wavelength, there is no need for a readjustment of the difference angle between both experiments with every scattering angle. Thus, the experiment requires fewer adjustment controls and promises an easier alignment compared with the two-colour set-up. The wavelengths used in the two-colour scheme cannot be chosen arbitrarily when the employment of a single transmission achromate is desired. On the one hand, the wavelengths should be close to the design wavelength of the achromatic lens in order to minimize spherical aberration. On the other hand, large wavelength differences call for large difference angles, that is a large clear aperture of the transmission achromate. These limitations again are overcome using the three-dimensional scheme. In addition, as there are no wavelength restrictions, a very long wavelength can be used in order to reduce the multiple-scattering probability by taking advantage of the wavelength dependence of the scattering cross-section.

Since its first suggestion [4] and an introduction of the components used by us [13], the successful deployment of a three-dimensional cross correlation set-up has been reported from different groups [14–16], together with promising applications [17, 18].

3. Theoretical remarks concerning three-dimensional cross correlation experiments

3.1. *Intercept*

In general, for the evaluation of light-scattering experiments the normalized intensity correlation function according to

$$g_{ij}^{I}(\tau) = \frac{\langle I_i(0) I_j(\tau)\rangle}{\langle I_i\rangle\langle I_j\rangle} \tag{3}$$

is used, where the indices $i = j = 1$ indicate an autocorrelation function and $i = 1$, $j = 2$ a cross correlation function. As we are dealing with coherent light experiments, the physics of the fluctuations is contained in the (electric) field correlation function

$$g_{ij}^{E}(\tau) = \frac{\langle \mathbf{E}_i(0) \cdot \mathbf{E}_j^*(\tau)\rangle}{\langle \mathbf{E}_i\rangle \cdot \langle \mathbf{E}_j^*\rangle}, \tag{4}$$

which is, however, in general not a measurable quantity. The connection between the intensity correlation function and the field correlation function is given by the Siegert relation

$$g_{ij}^{I}(\tau) = 1 + \beta |g_{ij}^{E}(\tau)|^2, \tag{5}$$

where β is called the intercept of the correlation function. Equation (5) is valid for complex circular Gaussian fluctuations of the electric field vector, meaning that the phase and the magnitude of the scattered field are statistically independent and zero mean Gaussians respectively. In this case, β can adopt a maximal value of unity, which is reduced by different effects, which we shall discuss in some detail in the following sections. As $g_{ij}^{I}(\tau)$ exhibits a variation of $g_{ij}^{I}(0) - g_{ij}^{I}(\infty) = \beta$ only, we are lead to call β the signal-to-noise ratio of a given dynamic light-scattering experiment.

A cross correlation function is obtained by feeding the signals from two different detectors into the electronic correlator. For simplicity, we disregard in this contribution any peculiarities concerned with photon counting and denote the measured signal the 'intensity'. According to equation (5), we write the measured intensity cross correlation function as

$$g_{12}^{I}(\tau) = 1 + \beta_{\mathrm{dec}}\beta_{\mathrm{opt}} |g_{12}^{E}(\tau)|^2, \tag{6}$$

with β_{dec} the degree of decorrelation due to multiple scattering and $\beta_{\mathrm{opt}} = \bar{\beta}_{\mathrm{coh}}\bar{\beta}_{\mathrm{non}}\beta_{\mathrm{jus}}\beta_{\mathrm{ov}}\beta_{\mathrm{P}}$. The meaning of the individual factors we shall now discuss separately.

3.1.1. *The coherence of detection*

If coherent light is directed on a spatially inhomogeneous sample, a granular pattern called speckles is formed. This pattern reflects the constructive and

Downloaded By: [Carl Zeiss AG] At: 12:49 11 November 2009

destructive interference of the light scattered by the sample. Its characteristic dimensions are given by the imaging optics, which is the human eye by direct observation. Note in passing that this gives rise to a nice optical effect upon head movement; for far-sighted people the observed speckle pattern seems to move in the same direction, whereas near-sighted people notice an opposite movement.

In a classical pinhole experiment, the area A of the second pinhole is chosen to be of the order of the characteristic dimensions l of the speckle pattern formed by the first pinhole (or the transmission lens); l^2 is frequently called the coherence area. If one chooses $A > l^2$, intensity is gained; however, this is at the expense of a reduction in β. Instead of the full modulation of the fluctuating signal, the detector now collects a reduced fluctuation superimposed to a background given by the degree of averaging determined by the pinhole. The effect is well known and has been discussed in detail, for example, by Rička [19], who aimed to remedy things by introducing the single-mode fibre as the light receiver. The main advantage of the single-mode fibre receiver is that the speckle concept loses importance as the fibre by itself selects the right mode emitted from the sample. It thus always guarantees the maximal intercept possible.

As we are dealing with cross correlation experiments, the coherence of both individual detection systems has to be taken into account, a fact which we denote by the bar in $\bar{\beta}_{\text{coh}}$. A typical value for a pinhole detection system is $\bar{\beta}_{\text{coh}} \approx 0.9$, whereas the single-mode fibre receiver always achieves the optimal value $\bar{\beta}_{\text{coh}} = 1$.

3.1.2. *Detector nonlinearities*

As discussed in detail by Flammer and Rička [20], the indirect effects of detector nonlinearities lead to a reduction in the measured intercept. This effect can be visualized by noting that nonlinear effects reduce the modulation of the (Gaussian) fluctuations of the sample. Again, the bar denotes a certain averaging over both detectors; typical values are expected to be $\bar{\beta}_{\text{non}} \approx 0.9$ for moderate count rates [21].

3.1.3. *Effect of the alignment*

In experiments for the decorrelation of multiple scattering with its two light paths, there are two scattering volumes, one for each independent experiment. In order to achieve a large signal-to-noise ratio, both scattering volumes have to be brought into the closest overlap. Schätzel has shown quantitatively [4] the importance of this factor; in particular, he derived a formula for the case of incident Gaussian beams of radius R, which reads

$$\beta_{\text{jus}} = \exp\left(-\frac{\delta^2 q R^2}{4}\right) \exp\left(\frac{\delta^2 x}{-R^2}\right), \tag{7}$$

where δq and δx are the deviations of both experiments with respect to each other in reciprocal and real space respectively. These deviations are due to insufficient alignment or possibly due to undiscovered differences in the experiments wavelengths. We shall return to this point in detail.

3.1.4. *Geometrical restrictions of the overlap volume*

The optimal overlap volume of both experiments is restricted by the geometry of the set-up and depends on the difference angle δ_{3D} only. In order to illustrate

Downloaded By: [Carl Zeiss AG] At: 12:49 11 November 2009

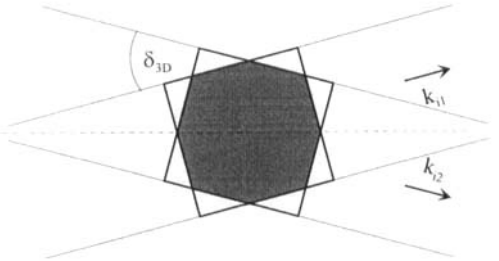

Figure 2. Sketch of the overlap regions of the incoming beams. A projection of the x–z plane is shown. For $\theta_g = 90°$, the shaded regions also represent the scattering volumes. The darkly shaded region indicates the overlap volume of the scattering volumes of both experiments.

Downloaded By: [Carl Zeiss AG] At: 12:49 11 November 2009

this, in figure 2 a sketch of the scattering volumes for the special case when $\theta_g = 90°$ is shown. The measured intercept is related to the scattering volumes by

$$\begin{aligned}\beta_{ov} &= \frac{\langle I_1^{ov}\rangle\langle I_2^{ov}\rangle}{\langle I_1\rangle\langle I_2\rangle} \\ &= \frac{V_{ov}^2}{V_1 V_2} \\ &= \left[\tan\left(\frac{\delta_{3D}}{2}\right) + \tan\left(\frac{\pi/2 - \delta_{3D}}{2}\right)\right]^2. \end{aligned} \tag{8}$$

The third equation can be derived by straightforward geometric considerations.

We here notice an additional advantage of the three-dimensional set-up compared with the two-colour set-up, where the difference angle has to be increased with increasing θ. According to the second term in equation (8), this leads to an angular dependence of the measured intercept in the two-colour case.

3.1.5. *Procedural influence*

This section describes a deficiency of a three-dimensional set-up compared with the two-colour experiment. The former exhibits only a maximal intercept of $\beta_P = 0.25$, whereas the latter shows the desired $\beta_P = 1$. This is because using two-colour coding the independent experiments are effectively separated using narrow-bandwidth filters, whereas in the three-dimensional case nothing hinders the light aimed for experiment 1 to appear in experiment 2 and vice versa.

In writing down the cross correlation function, these contributions have to be taken into account:

$$G_{12}(\tau) = \langle I_1^{i}(0) I_2^{i}(\tau)\rangle + \langle I_1^{i}(0) I_2^{ii}(\tau)\rangle + \langle I_1^{ii}(0) I_2^{i}(\tau)\rangle + \langle I_1^{ii}(0) I_2^{ii}(\tau)\rangle, \tag{9}$$

where the subscripts 1 and 2 denote the detectors whereas the superscripts i and ii denote the lasers (or wavelengths).

Let us start with the two-colour experiment, for which $G_{12}^{2C}(\tau) = 0 + \langle I_1^{i}(0) I_2^{ii}(\tau)\rangle + 0 + 0$ is obtained. The zeros result because the light of the wrong wavelength is blocked by the filters in front of the detectors. Normalization according to equation (3) then gives

$$g_{12}^{2C}(\tau) = \frac{\langle I_1^{i}(0) I_2^{ii}(\tau)\rangle}{\langle I_1^{i}\rangle\langle I_2^{ii}\rangle} = 1 + 1\frac{\beta}{\beta_P}|g_{12}^{E}(\tau)|^2. \tag{10}$$

In the case of a three-dimensional experiment, equation (9) is still valid. However, in the third term the orientations of the $\mathbf{q}_i$ differ while, in the first and the fourth term, the $\mathbf{q}_i$ even differ in magnitude. Therefore, only the second term gives a correlated contribution. Upon normalization, one gets

$$g_{12}^{3D}(\tau) = \frac{G_{12}^{3D}(\tau)}{\langle I_1^{i} + I_1^{ii}\rangle\langle I_2^{i} + I_2^{ii}\rangle} = \frac{3\langle I_1\rangle\langle I_2\rangle + \langle I_1^{i}(0) I_2^{ii}(\tau)\rangle}{4\langle I_1\rangle\langle I_2\rangle} = 1 + \frac{1}{4}\frac{\beta}{\beta_P}|g_{12}^{E}(\tau)|^2. \tag{11}$$

It is instructive to perform the same calculation for the Phillies experiment. As Schätzel [4] pointed out, in general the Siegert relation (equation (5)) reads

$$g_{12}^{I}(\tau) = 1 + \beta\left(\left|\frac{\langle \mathbf{E}_1(0)\cdot\mathbf{E}_2^{*}(\tau)\rangle}{\langle \mathbf{E}_1\rangle\cdot\langle \mathbf{E}_2\rangle}\right|^2 + \left|\frac{\langle \mathbf{E}_1(0)\cdot\mathbf{E}_2(\tau)\rangle}{\langle \mathbf{E}_1\rangle\cdot\langle \mathbf{E}_2\rangle}\right|^2\right), \tag{12}$$

where the second term has to be used in cross correlation experiments with opposing beams, that is $\mathbf{q}_1 = -\mathbf{q}_2$, whereas the first term is used otherwise ($\mathbf{q}_1 = \mathbf{q}_2$). The Phillies scheme now relies on two experiments with $\mathbf{q}_1 = -\mathbf{q}_2$. However, comparable with the three-dimensional scheme, light from the 'wrong' experiment contributes to the intensity at a given detector. In addition, both 'wrong' experiments themselves give a correlated contribution. Therefore, following the reasoning above yields the result

$$g_{12}^{PH}(\tau) = \frac{G_{12}^{PH}(\tau)}{\langle I_1^{i} + I_1^{ii}\rangle\langle I_2^{i} + I_2^{ii}\rangle} = \frac{2\langle I_1\rangle\langle I_2\rangle + \langle I_1^{i}(0) I_2^{ii}(\tau)\rangle + \langle I_1^{ii}(0) I_2^{i}(\tau)\rangle}{4\langle I_1\rangle\langle I_2\rangle} = 1 + \frac{1}{2}\frac{\beta}{\beta_P}|g_{12}^{E}(\tau)|^2. \tag{13}$$

This means that the cross correlation function measured with the Phillies arrangement is *not* the same as with an autocorrelation experiment, in contrast to the statement by Phillies [3]. The difference is that two correlation functions, corresponding to $\theta'' = \theta' - 180°$, have to be added for both experiments, which are obviously identical in the symmetrical case of $\theta_1 = \theta_2 = \theta' = -\theta'' = 90°$ only; θ' refers to the intended experiment, and θ'' to the 'wrong' experiment. In this case, because two correlation functions contribute, the intercept is twice the value obtained for a three-dimensional experiment. (Note that this discussion also invalidates the estimate for the cross correlation intercept by Mos *et al.* [10].)

Downloaded By: [Carl Zeiss AG] At: 12:49 11 November 2009

We note in passing that this reveals the feasibility of another cross correlation scheme, which has not yet been described. If, using the Phillies arrangement, both detectors are rotated synchronously such that always $\theta_1 = \theta_2$ (e.g. using a common detector arm), the measured cross correlation function will be a sum of two correlation functions at different q, that is in the previous notation, one with $q_1 = q_2 = q(\theta')$ and another with $q_1 = q_2 = q(\theta'')$, both having a maximal intercept of $\frac{1}{4}$. This sum can be calculated in principle. However, as the respective weights of both correlation functions will in general depend on the scattering angle, this possibility seems to be of minor importance and calls for the employment of the time-coding proposal [4].

In conclusion, β_P equals 1, $\frac{1}{4}$ and $\frac{1}{2}$ for the two-colour, three-dimensional and Phillies cross correlation schemes respectively.

3.1.6. *Efficiency of multiple-scattering decorrelation*

It has been shown by Schätzel [4] that the efficiency η of the decorrelation of double scattering depends on the 'difference' of the two independent experiments according to

$$\eta = 1 - \frac{\langle \mathbf{E}_1^{(d)}(0) \cdot \mathbf{E}_2^{(d)}(\tau)^* \rangle}{\langle \mathbf{E}_1^{(d)}(0) \cdot \mathbf{E}_1^{(d)}(\tau)^* \rangle}$$

$$= 1 - \frac{(\pi/2)^{1/2}}{R|\mathbf{k}_1 - \mathbf{k}_2|}, \tag{14}$$

where the superscript (d) denotes double scattered light. R is the Gaussian radius of the incident beams and $|\mathbf{k}_1 - \mathbf{k}_2| = (4\pi n/\lambda) \sin(\delta_{3D}/2)$. This leads to an optimal difference angle in a three-dimensional cross correlation experiment, which is given by the trade-off between the multiple-scattering decorrelation efficiency and the overlap of both scattering volumes (cf. section 3.1.4). This trade-off is shown in figure 3, from which an optimal difference angle of approximately $\delta_{3D} = 5°$ can be taken. Owing to the decrease in the intercept with difference angle this gives a maximal intercept of $\beta_{ov}\beta_P = 0.23$. Note that η is fixed by the set-up and is not related to β_{dev} from equation (6), which describes the relative amount of single scattering events (indicated by the superscript (s)) in relation to all scattering events:

$$\beta_{dec} = \frac{\langle I_1^{(s)} \rangle \langle I_2^{(s)} \rangle}{\langle I_1 \rangle \langle I_2 \rangle}. \tag{15}$$

Under the approximation $\eta = 1$, this relation may be used to correct static light scattering data for multiple scattering.

3.2. *Polarization*

We finish this theoretical section by considering a rather peculiar behaviour found only in three-dimensional light scattering set-ups. The scattering plane of an individual experiment does not include a fixed angle with the plane of symmetry of both experiments. This can be visually explained by regarding two extremal cases. For the goniometer angle $\theta_g = 0°$, the tilt angle Δ between a scattering plane and the plane of symmetry equals the difference angle, that is $\Delta = \delta_{3D}/2$, whereas with the goniometer angle $\theta_g = 180°$ the tilt angle changes to $\Delta = 90°$. This tilting

Downloaded By: [Carl Zeiss AG] At: 12:49 11 November 2009

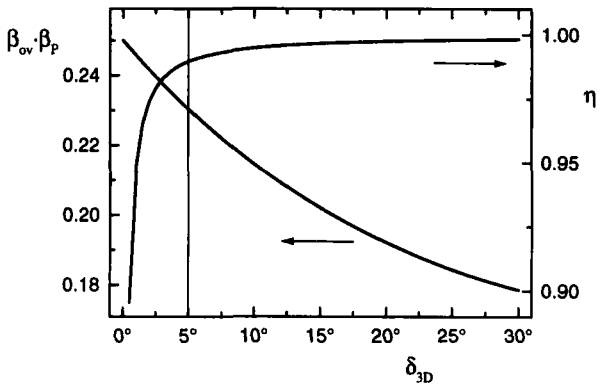

Figure 3. Theoretical intercept $\beta_{ov}\beta_P$ and efficiency of multiple-scattering decorrelation η as a function of the difference angle δ_{3D}. The 'optimal' difference angle is indicated by the vertical line.

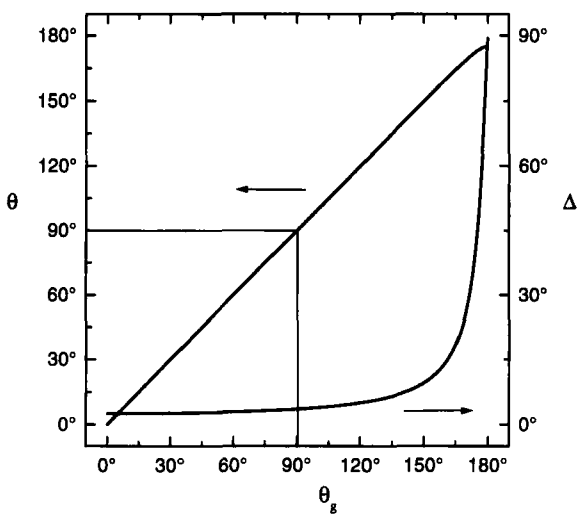

Figure 4. Tilting angle Δ and scattering angle θ as functions of the goniometer angle θ_g.

of the scattering planes with goniometer angle also influences the scattering angle θ, which is, in general, *not* equal to the goniometer angle θ_g. We leave the derivation of the according equations to appendix A. The result is shown in figure 4, from which it becomes evident that the mentioned distinction made between the scattering angle θ and the goniometer angle θ_g noticeably matters above $\theta_g \approx 150°$ only.

The tilting of the scattering planes with respect to the plane of symmetry has a very important consequence, however. As the polarization of the incident beam is only fixed with respect to the plane of symmetry, an artificial depolarization is observed above $\theta_g \approx 150°$. This is shown in figure 5, where the notation V_V corresponds to the usual polarized light scattering experiment with vertical incident polarization and vertical orientation of the analyser, while V_H corresponds to a depolarized experiment with horizontal orientation of the analyser. Note that at large goniometer angles the polarization of the scattered light is still linear, but a

Downloaded By: [Carl Zeiss AG] At: 12:49 11 November 2009

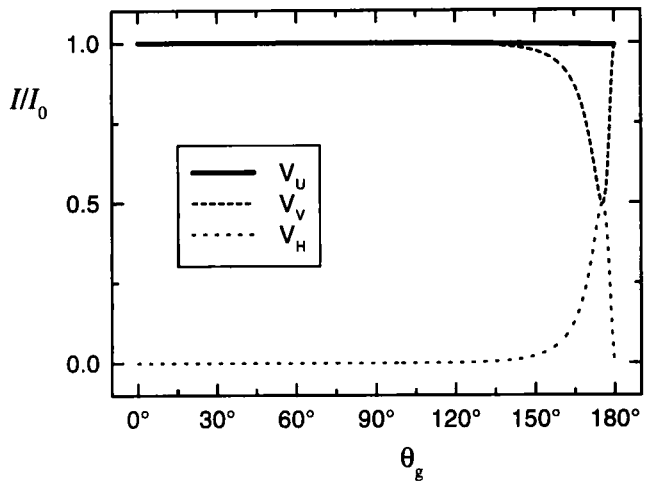

Figure 5. Scattered intensities as a function of the goniometer angle θ_g for different polarization components indexed as follows: V, incident polarization inclined by $\delta_{3D}/2$ with respect to the plane of symmetry or analyser perpendicular to the plane of symmetry; H, analyser parallel to the plane of symmetry; U, no analyser present; V_U is the sum of the V_V and V_H components.

depolarized component is present if polarizer and analyser are kept fixed, the amount of which (or the necessary respective polarizer and analyser rotation) can be calculated with the help of the formula given in the appendix.

For the investigation of depolarizing (e.g. optical anisotropic) samples this feature is a clear disadvantage of the three-dimensional set-up.

4. Characterization of the set-up realized in our laboratory

Figure 6 shows both a side and a top view of the set-up realized in our laboratory. The light of two semiconductor lasers is coupled into polarization-maintaining single-mode fibres. The outgoing light is directed onto a transmission lens ($f' \approx 200\,\text{nm}$) parallel to its optical axis. Both respective distances from the optical axis are chosen to be identical, in order to guarantee the same incident angle on the sample for both incident light beams. This angle is chosen to $\delta_{3D}/2 = 2.5°$, the optimal value. An identical detection lens guarantees a symmetrical optical set-up. The scattered light is coupled into a single-mode fibre, which assures a high intercept as already noted. The detectors that we use are silicon avalanche photodiodes with a gated quenched circuit, the merits of which have already been published [21]. Their TTL signals are fed into a digital correlator (ALV-5000/E).

The coupler and the lens on the transmission side are fastened to a large aluminium frame. The same is true for the detection side, where a home-built goniometer is constructed using a gear driven by a stepper motor; the resolution of the stepper motor is 0.02°. The sample is fixed to a similar gear and a stepper motor, which allows a rectangular cuvette to be rotated in $\theta/2$–θ geometry. An additional fixing allows the use of cylindrical cuvettes.

In the following sections we shall describe some features of the set-up.

Downloaded By: [Carl Zeiss AG] At: 12:49 11 November 2009

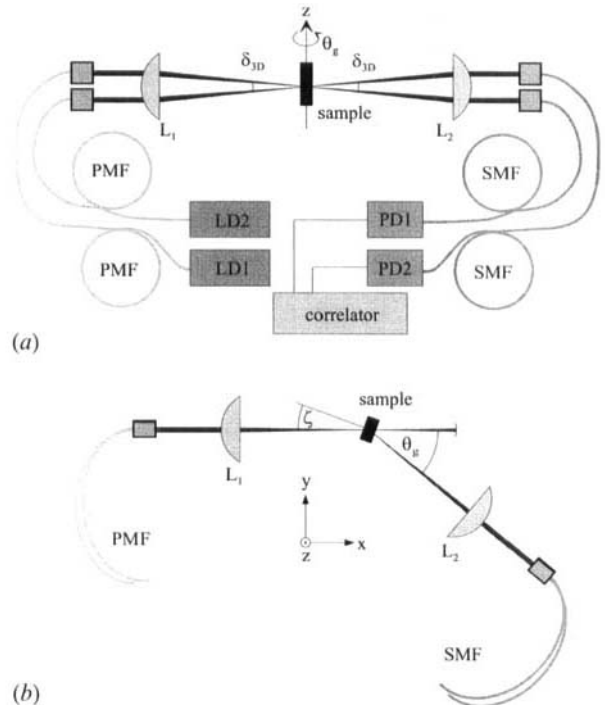

Figure 6. Scheme of the three-dimensional set-up: (*a*) side view, $\theta_g = 0$; (*b*) top view, $\theta_g \neq 0$. For details see text. LD, laser diodes; PD, avalanche photodiodes, PMF, polarization-maintaining fibres; SMF, single-mode fibres; L_1, L_2, transmitting and receiving lenses.

4.1. *Semiconductor diode lasers*

As the light source for both experiments we use $Ga_{1-x}Al_xAs$ semiconductor lasers (Mitsubishi ML 64114R), which deliver 50 mW light power at an operating current of 140 mA; the threshold current is 50 mA. The diodes are specified for both single-transverse- and single-longitudinal-mode output at a wavelength $\lambda = 790$ nm at 24°C; for a light power of below 20 mW, additional longitudinal modes are expected. The diodes are fixed in a copper block which is cooled by a Peltier element to within $\Delta T = 0.02$ K. Both the voltage supply and the Peltier element driver are home-built. The laser light is coupled into a polarization-maintaining single-mode fibre, the coupler being directly attached to the copper block. The mechanical set-up and the fibres were supplied by OZ Optics, Canada, who also performed the laser-to-fibre coupling. Coupling losses result in a fibre output power of approximately 25 mW; power fluctuations are less than 5‰. The polarization cross-talk is specified to be 18 dB; we measured a cross-talk of approximately 16 dB applying a 30 dB near-infrared polarizer (Corning, USA). This value is comparable with those of commercial gas lasers.

In order to check the single-longitudinal-mode behaviour of the diodes we determined their coherence lengths with a Michelson interferometer. A coherence length larger than 4 m was determined. We note that this is a lower limit because of the difficulties in observing the interference fringes visually.

Diode lasers are known to change their oscillating wavelength upon variation in their operation temperature [22]. This is, to a smaller proportion, due to the

Downloaded By: [Carl Zeiss AG] At: 12:49 11 November 2009

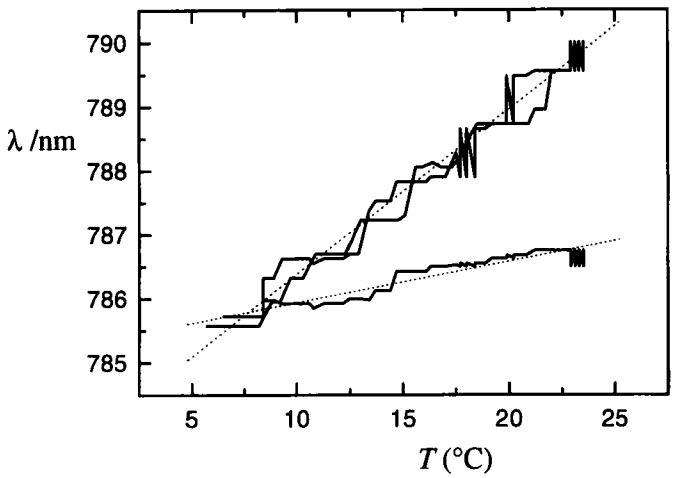

Figure 7. Semiconductor laser wavelength as a function of operating temperature. Steeper lines are the uncorrected laser wavelength data for both lasers; flatter line is the wavelength change of one laser with correction for the mode hops; dotted lines are linear fits to the data.

Downloaded By: [Carl Zeiss AG] At: 12:49 11 November 2009

increase in the optical path length of the laser cavity with increasing temperature because of thermal expansion of the laser crystal. The main effect, however, is a shift of the gain profile with temperature. To a certain degree, these effects can be taken advantage of as the wavelength of the laser can be continuously tuned with temperature. However, there exist instability points, where a mode hop occurs, which alters the wavelength discontinuously by approximately $\Delta\lambda = 0.35\,\text{nm}$. This value is given by the refractive index of $Ga_{1-x}Al_xAs$ and the typical cavity length of the semiconductor crystal of 250 μm.

As explained above, for a cross correlation experiment it is essential that the incident wavelengths of the two lasers differ as little as possible. We therefore measured the wavelength of both lasers with a high-resolution spectrometer, using a reflection grating with a grating period of $1.2\,\mu\text{m}^{-1}$ and employing an arm length of approximately 5 m. We thereby achieve an accuracy of $\delta\lambda = 0.1\,\text{nm}$. A measurement of the wavelength variation of both lasers as a function of their operation temperature is shown in figure 7. Two different slopes can be identified. The steeper slope is determined to be $0.25\,\text{nm}\,\text{K}^{-1}$. If one corrects for the occurrence of mode hops by simply ignoring the theoretically expected wavelength jump, a less steep slope of $0.06\,\text{nm}\,\text{K}^{-1}$ is obtained. Both values are in agreement with those reported by Wieman and Hollberg [22] for the temperature coefficient in the shift of the gain profile and the thermal expansion of the optical cavity, respectively. According to figure 7, we operate our lasers at the plateau value at approximately 19°C and fine tune the temperature until both wavelengths are the same within the accuracy of our spectrometer. This results in a common wavelength of $\lambda = 788.7\,\text{nm}$.

4.2. *Optical components*

Transmission and detection lens constitute an afocal telescopic system with magnification −1 if aligned to common focal points. We use planoconvex singlets made from BK7 ($n = 1.511$ at $\lambda = 790\,\text{nm}$) with a radius of 104.41 mm and a

thickness of 8 mm. Planoconvex singlets have its first principal plane H located at the lens vertex, to which all distances refer; H′ is located for our lenses at 2.7 mm. Their effective focal length is $f' = 204.3$ mm; their clear aperture is 61 mm. With an incident beam parallel to the optical axis the main optical error is spherical aberration, which shifts the focal point in the axial direction by −8 mm if the full aperture is used. Spherical aberration of the lens system is substantially reduced (the longitudinal aberration by a factor of four), if the lenses are both mounted with their curved surfaces directed outwards, as sketched in figure 6. However, spherical aberration does not really matter in our set-up as the positions of the incoming and scattered beams with respect to the optical axis are fixed and the alignment guarantees the confocal arrangement of the singlets.

The fibre couplers are equipped with an aspheric lens of focal length $f' = 3.9$ mm. The outgoing beam is diffraction limited with a diameter of 0.8 mm, leading to a divergence angle of 1.25 mrad. This small divergence leads to a small but non-zero comatic aberration of the optical set-up; astigmatism is negligible.

The Gaussian beam parameters were calculated for an axial beam with the parameters above located at −35 mm from the lens vertex of the planoconvex singlet. We obtain a Rayleigh range of approximately 60 nm, thus facilitating the alignment of the focal points. The beam waist radius is $R = 125\,\mu$m, located at 190 mm, and the full angle divergence is 4 mrad.

4.3. *Mechanical components and alignment*

The transmission as well as the detection lens are fixed to three translation stages which allow for the movement in the three translational degrees of freedom. The fibre couplers on both sides are again fixed to two translation stages for y–z movements. The coupler itself permits the alignment of the Euler angles of the coupling lens. The assembly consisting of the fibre coupler and the translation stages is connected to the lens frame. This allows for a movement of the complete optical system (lens and two fibre couplers) with respect to the reference frame in every spatial direction (x, y, z) without deterioration of the alignment. All translation stages have a reproducibility of $\delta x = 10\,\mu$m. Besides the manufacturing tolerances, no care is taken to verify that the optical axis of the transmission and detection lens and the axis of rotation of the goniometer are perpendicular. The same applies for the axes of rotation of the sample and the goniometer.

Briefly, the alignment procedure runs as follows. Without insertion of the transmission and the detection lenses, the incident laser beams are adjusted to aim at the rotation axis parallel to the plane of rotation of the goniometer by means of a horizontal and a vertical adjustment needle. The detection side fibre couplers are then adjusted until they pick up the maximal intensity of the direct incident light. Now, the transmission lens is inserted, followed again by verification of whether the beams still hit the rotation axis. Afterwards, the index-matching vat is inserted and filled with water. Again both beams have to hit the rotation axis. Alignment has to be checked, in addition, so that the lens foci are located on the rotation axis. The detection lens is inserted, and again the translation stages on the detection side are adjusted for maximum light coupling into the detection fibre. Fune tuning is achieved by optimizing the intercept by a translation of the index-matching vat and the whole lens-coupler units.

Downloaded By: [Carl Zeiss AG] At: 12:49 11 November 2009

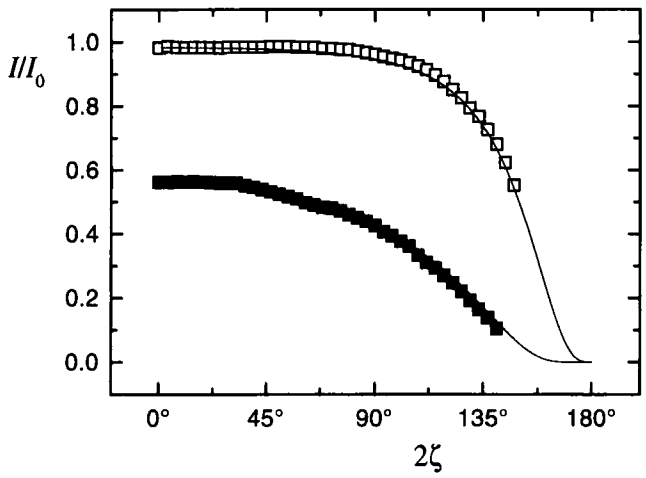

Figure 8. Normalized transmitted intensity of a rectangular cuvette ($d = 1$ mm) as a function of the angle 2 ζ of the cuvette's normal with the incident light: (□), cuvette filled with water; (■), cuvette filled with an aqueous sample of turbidity $\tau = 0.6\,\text{mm}^{-1}$; (—), calculations according to equations (B 2) and (B 3).

Downloaded By: [Carl Zeiss AG] At: 12:49 11 November 2009

4.4. *Rectangular cuvettes*

As long as the photon mean free path is larger than the characteristic dimensions of the scattering volume, the amount of multiply scattered light present can be reduced by decreasing the optical path length within the cuvette. Decreasing the diameter of a cylindrical cuvette, however, leads to strong distortions of the optical system as the increasing diopter of the related cylindrical lens leads to strongly increasing astigmatism. This disturbance can be prevented by employing rectangular cuvettes in a $\theta/2$–θ geometry, meaning that the cuvette's window normal includes an angle of $\zeta = \theta/2$ with the incident beam direction. Upon changing the scattering angle θ (or, more exactly, θ_g) the cuvette has to be rotated accordingly. Owing to refraction, this symmetric arrangement leads to a shift in the overlap volume of the two scattering experiments parallel to the cuvette's windows only, without any influence on the overlap and thereby on β_{opt}. In this way, cuvettes of very small thickness can be used in order to achieve a reduction in the multiple-scattering contributions.

There are two different optical effects present, which lead to a nonlinear correction for the transmission (or, equivalently, for the light intensity incident on the scattering volume) with scattering angle. First, the transmission for linear polarized incident light changes in accordance with the Fresnel formulae and, second, the optical path length within a given cuvette changes upon rotation of the cuvette. Both effects are depicted in figure 8, where the transmitted light as a function of the rotation angle ζ of the cuvette is shown. Two situations are evaluated: the cuvette filled with water, and, in addition, the cuvette filled with a strongly scattering sample, which was a suspension of colloidal spheres with nominal radius of $r = 57.5$ nm and 1% solid content. The same sample is used again below. The theoretical expectation can be derived from the Fresnel formulae (B 1) and the Lambert–Beer law (B 3) and is given in appendix B. The measured data follow closely the theoretical lines; this is, as far as the turbid sample is

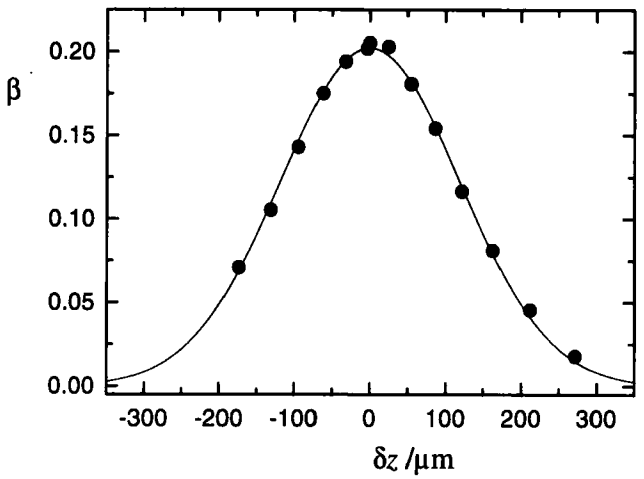

Figure 9. Variation in the intercept β as a function of a mismatch δz of the scattering volumes: (—), fit according to equation (7) (for details see text).

Downloaded By: [Carl Zeiss AG] At: 12:49 11 November 2009

concerned, another nice way to demonstrate the validity of the Lambert–Beer law at that turbidity.

While these effects lead to corrections for static measurements only, we found a comparable strong variation in the intercept β_{opt} upon variation in the cuvette angle with fixed θ_g. The effect can be quantitatively explained by assuming a geometrical misalignment of the detection light paths with respect to the incident light beams away from the symmetry angle $\zeta = \theta/2$.

4.5. *Check of experimental performance*

In order to assess that every relevant parameter influencing the intercept of the cross correlation function has been identified, we checked its behaviour under different alignment situations.

First we examined whether equation 7 is a sufficient description of the variation in the signal-to-noise ratio with alignment parameters. We used a strongly dilute ($\phi \approx 10^{-3}$) sample of polystyrene latex spheres with small radii ($r < 50\,\text{nm}$), which should give no multiple scattering ($\beta_{dec} = 1$) and no angular variation in the scattered intensity. In figure 9 we show the measured dependence of the intercept on a spatial mismatch of the scattering volumes. This mismatch has been achieved by inserting a glass plate into one illumination beam and tilting it. For small tilting angles, this procedure lifts one beam with respect to the other, thereby introducing a spatial mismatch δz of the scattering volumes. The solid curve in figure 9 is a Gaussian according to equation (7), the only fitting parameter being the Gaussian beam radius R, which is obtained as $R = 168\,\mu\text{m}$, in reasonable agreement with the calculated value of $R = 125\,\mu\text{m}$ (cf. section 4.2). The maximal intercept results from the fit to $\beta = 0.20$; however, we do not refer to it as a fitting parameter, as we are able to calculate it from the experimentally know deviation from ideal alignment. Recall from equation (7) that β_{jus} is given by a product of two Gaussians originating from spatial and wave-vector mismatch. We are probing the first type of mismatch here, at least in one spatial dimension; the second type of mismatch can be calculated using a corresponding error progression, which yields

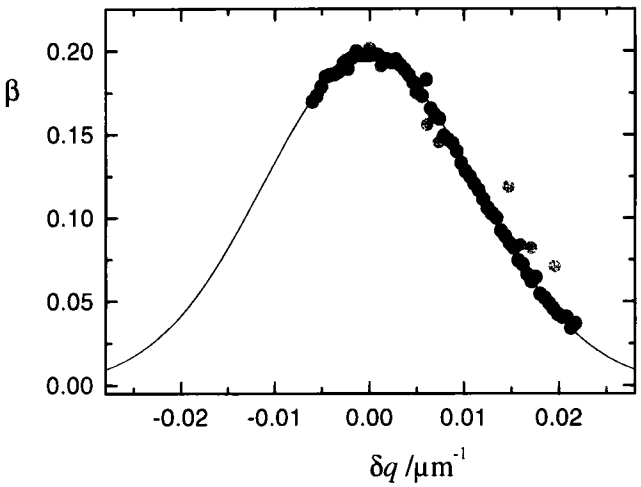

Figure 10. Variation in the intercept β as a function of a mismatch δq of the scattering vectors: (●), data obtained by adjustment of the receiving optics; (●), data obtained by tuning the wavelength of one of the diode lasers; (—), fit according to equation (7) (for details see text).

$$\delta q = \frac{4\pi n\,\delta\lambda}{\lambda^2}\sin\left(\frac{\theta}{2}\right) + \frac{2\pi n\,\delta\theta}{\lambda}\cos\left(\frac{\theta}{2}\right). \tag{16}$$

From equation (6) we know that the measured intercept under optimal alignment conditions β_{opt} can be calculated using the following individual contributions: $\bar{\beta}_{coh} = 1$, as we use single-mode fibre receivers; $\bar{\beta}_{non} = 0.9$ owing to slight non-linearities of our detectors at the count rates that we used; $\beta_{ov}\beta_P = 0.23$ (cf. section 3.1.6). The remaining β_{jus} can be calculated as follows. The resolution of our spectrometer determines the wavelength uncertainty in our experiment to be $\delta\lambda = 0.1$ nm; $\delta\theta = 5 \times 10^{-5}$ has been estimated using the tangent of $\delta y = 10\,\mu$m, the reproducibility of the translation stages, divided by the focal length of the detection lens ($f' = 204$ mm). The measurements shown in figure 9 were performed at $\theta_g = 54°$; using a Gaussian beam radius of $R = 125\,\mu$m, the result for β_{jus} due to a mismatch in q is $\beta_{jus}(\delta q) = 0.994$; the two spatial dimensions add a contribution of $\beta_{jus}(\delta x, \delta y) = 0.987$, where again the reproducibility of our translation stages has been used. With this we calculate the maximal intercept attainable in the measurements shown (figure 9) to be $\beta_{opt} = 0.203$ which is, within the fitting errors, exactly the value that we find experimentally.

Following this line, we consequently show in figure 10 the measured dependence of the intercept from a difference δq in the scattering vectors. The grey full circles were obtained by tuning the wavelength of one laser, calculating δq by assuming that $\delta\theta = 0$; the black full circles were obtained by shifting one fibre coupler on the detection side by a certain amount δy, thereby introducing a known mismatch of the scattering angles. Again, the fitting curve is a Gaussian according to equation (7), and the Gaussian beam radius, as the only fitting parameter, is obtained to be $R = 125\,\mu$m, identical with the calculated value. The maximum intercept can be calculated as above to be $\beta_{opt} = 0.203$, where

Downloaded By: [Carl Zeiss AG] At: 12:49 11 November 2009

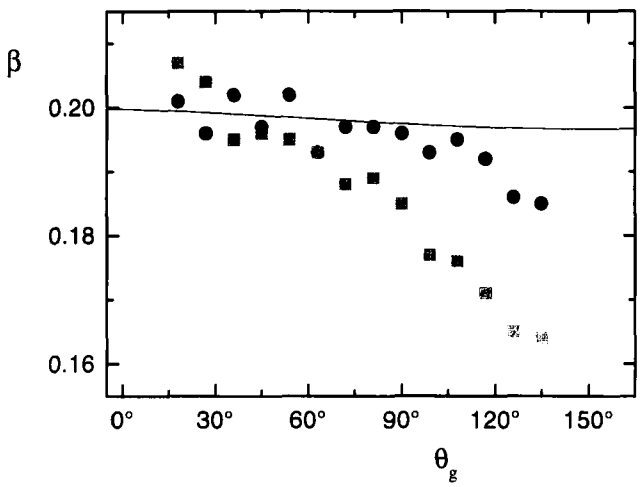

Figure 11. Variation in the intercept β as a function of the goniometer angle θ_g, where the sample is a strongly diluted suspension of polystyrene spheres ($r = 42.5$ nm; $\phi = 10^{-3}$): (●), measurements obtained in a cylindrical cuvette; (■), measurements obtained in a rectangular cuvette ($d = 1$ mm); (—), Gaussian error progression in λ and θ without adjustable parameters (for details see text).

$\beta_{jus}(\delta x, \delta y, \delta z) = 0.981$ has been used. Once more we establish exact agreement with the measurements.

In addition, we shall be able to verify whether the measured intercept is independent of the scattering angle as expected (cf. section 3.1.3). Our measurements, shown in figure 11, reveal the intercept as a function of the scattering angle after the alignment walk-in. No strong angular dependence is observed, thus confirming our expectation. The slight decrease visible for the cylindrical cuvettes (black full circles) is due to the already-mentioned deviation from ideal alignment. This is confirmed by drawing the Gaussian error progression of the alignment deviations (equation (7) together with equation (16)) as a solid line. As the data follow very closely this curve, we conclude that there remains no unresolved contribution which causes our measured signal-to-noise ratio to deteriorate. The stronger deviations, which are visible for the rectangular cuvettes (grey full squares), are presumably due to a deviation of the cuvette from the exact $\zeta = \theta/2$ position or from the difference between θ and θ_g.

Let us sum up these results by saying that our apparatus is characterized by an optimal intercept of approximately $\beta_{opt} = 0.20$. This value is fully understood and results from additive and unavoidable alignment errors, which are measured to be $\delta\lambda = 0.1$ nm, $\delta\theta = 5 \times 10^{-5}$ and $\delta x = \delta y = \delta z = 10\,\mu$m.

Finally, we investigated the dynamics of colloidal suspensions with different solid contents. We used polystyrene latex particles with a nominal transmission electron microscopy diameter $2r = 115$ nm (±4.7%), suspended in water with a high salt content (500 μmol dm^{-3} NaOH^{-3}) in order to avoid an influence of electrostatic interaction on the diffusion coefficient. We first measured a sample with $\phi = 1\%$ particle volume fraction, the turbidity of which was $\tau = d^{-1} \ln (I_0/I) = 0.6$ mm^{-1}. Note that such turbid samples do not readily follow the Lambert–Beer law of transmission.

Downloaded By: [Carl Zeiss AG] At: 12:49 11 November 2009

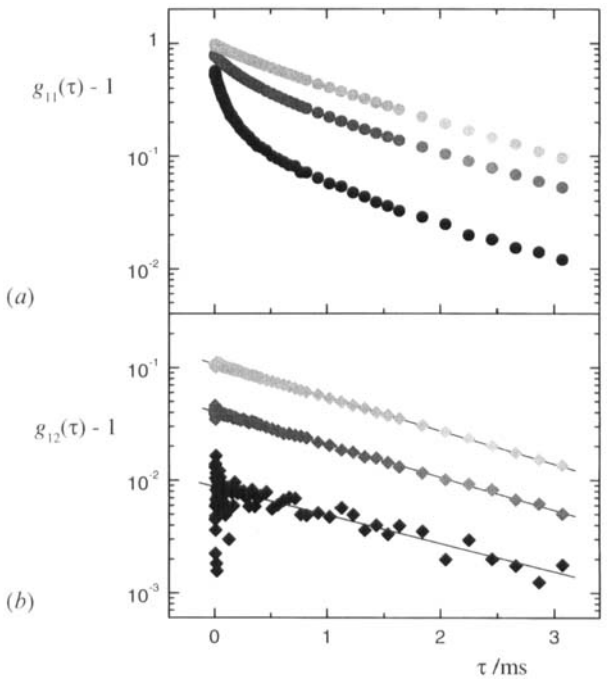

Figure 12. (*a*) Autocorrelation and (*b*) cross correlation functions of a turbid ($\tau = 0.6\,\mathrm{mm}^{-1}$) polystyrene latex sample, employing a scattering vector $q = 9.6\,\mu\mathrm{m}^{-1}$. The nominal particle radius is $r = 57.5\,\mathrm{nm}$, and the volume fraction is 1%. The parameter is the cuvette thickness which, from top to bottom, equals 1 mm, 5 mm and 10 mm respectively. The straight lines in the cross correlation plots are linear fits to the data, which yield respectively (from top to bottom) $\beta = 0.11$ and $r = 58.2 \pm 0.2\,\mathrm{nm}$, $\beta = 0.04$ and $r = 59.6 \pm 0.5\,\mathrm{nm}$, and $\beta < 0.01$ and $r = 69 \pm 4\,\mathrm{nm}$.

Figure 12 shows the autocorrelation function $g_{11}(\tau)$ and cross correlation function $g_{12}(\tau)$, which were obtained using three rectangular cuvettes with increasing thickness. The upswing in the autocorrelation functions is a clear manifestation of multiple scattering, the amount of which increases with increasing cuvette thickness. This also visible in the cross correlation functions, where the intercept decreases with increasing multiple-scattering contributions. The solid lines are linear fits to the data, from which the particle radius can be determined. The first two experiments using the thinner cuvettes ($d = 1\,\mathrm{mm}$ and $r = 58.2\,\mathrm{nm}$; $d = 5\,\mathrm{mm}$ and $r = 59.6\,\mathrm{nm}$) yield a radius which is in excellent agreement with the expected value, whereas the data obtained in the thick cuvette scatter strongly and the determined radius is far too large. We use this result as complementary information and state that care has to be taken in evaluating data with signal-to-noise ratios smaller than 1%.

Additional technical information can be read from the data in figure 12. First, every cross correlation data set shows a stronger data scatter towards smaller lag times. This is due to counting noise in the first correlator channels. Note that in the twentieth correlator channel (lag time $\tau = 4.8\,\mu\mathrm{s}$; sample time 400 ns), which is the first channel shown in figure 12, only 4×10^{-3} correlated counts appear in the top cross correlation function. Second, if nonlinear effects of the detectors are carefully excluded, β_{dec} can be obtained from the data. For the smallest cuvette

Downloaded By: [Carl Zeiss AG] At: 12:49 11 November 2009

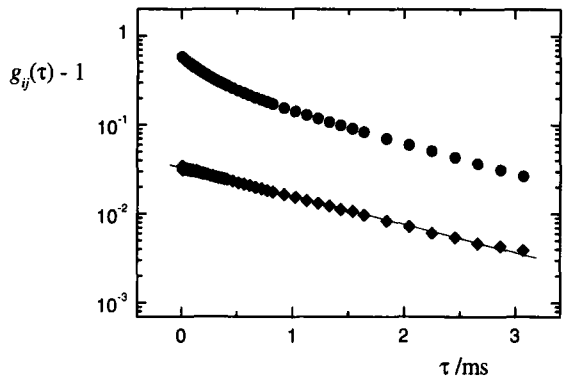

Figure 13. Autocorrelation (●) and cross correlation (◆) functions of a strongly turbid ($\tau = 3\,\mathrm{mm}^{-1}$) polystyrene latex sample, employing a scattering vector $q = 9.6\,\mu\mathrm{m}^{-1}$. The nominal particle radius is $r = 57.5\,\mathrm{nm}$, and the volume fraction is 5%. The cuvette thickness is 1 mm. The straight line in the cross correlation plot is a linear fit to the data, which yields $\beta = 0.03$ and $r = 54.5 \pm 0.3\,\mathrm{nm}$.

Downloaded By: [Carl Zeiss AG] At: 12:49 11 November 2009

thickness, $\beta = 0.11$ is obtained. As we expect $\beta_{\mathrm{opt}} = 0.20$ we might estimate $\beta_{\mathrm{dec}} = \beta/\beta_{\mathrm{opt}} = 0.6$, meaning that approximately 25% of the scattered light intensity is due to multiple scattering. Note in addition that the autocorrelation intercept of the sample in the smallest cuvette is approximately $\beta = 0.98$, a value which can only be obtained by single-mode fibre receivers; $\beta > 0.9$ is due to the exceptionally low count rate.

As we aimed to set up an apparatus which should be able to reach the limits of multiple-scattering cross correlation, we still increased the solid content of the sample. Figure 13 shows the autocorrelation and cross correlation functions of a sample of the same colloidal particles with a volume fraction $\phi = 5\%$, which results in the very high turbidity $\tau = 3\,\mathrm{mm}^{-1}$. The measurements were performed employing the 1 mm cuvette. To our knowledge, figure 13 shows results from the strongest turbid sample ever investigated by dynamic light-scattering techniques. Again, the radius can be obtained from a linear fit to the data. The value obtained ($r = 54.5 \pm 0.3\,\mathrm{nm}$) is slightly smaller than the expected value, which might indicate the beginning influence of hydrodynamic interaction or structure formation in the sample. With $q = 9.6\,\mu\mathrm{m}^{-1}$ and the volume fraction $\phi = 5\%$, we are well below $q_{\mathrm{max}} = 2\pi/a \approx 15\,\mu\mathrm{m}^{-1}$, where a is the mean particle spacing. In the case of ordering this would also be the position of the first maximum of the fluid structure factor. In both cases we therefore expect to measure colloidal collective short-time dynamics, for which a 7% increase in the diffusion coefficient is expected for hard spheres [23]:

$$\frac{D_{\mathrm{eff}}}{D_0} = 1 + 1.44\phi, \tag{17}$$

in accordance with our measurement. The intercept that we obtain is $\beta = 0.03$; with great caution, one might estimate as above that more than 60% of the detected light results from multiple-scattering processes.

Let us close this contribution with the following remarks. We have demonstrated the features of a versatile apparatus for the investigation of the dynamics of strongly turbid samples by dynamic light scattering. We think that the equipment that we introduced is superior to the commercially available two-colour set-up as it allows for the use of rectangular cuvettes and has no restrictions for choosing the laser wavelength. Taking advantage of both features we were able to measure the dynamics of the strongest turbid samples ever investigated by dynamic light scattering free from multiple-scattering distortions. For the first time it will be possible, therefore, to investigate the micellar dynamics of delicate emulsions from the life science industry or hydrodynamic interactions in strongly concentrated suspensions, both of which are not accessible by diluting or index matching the samples. The dependence of hydrodynamic interactions on the potential interaction in concentrated charge-stabilized suspensions is widely explored by theoretical means, but there exist only very rare experimental investigations. That is why we think that the method described in this contribution will make dynamic light-scattering experiments of strongly scattering samples increasingly popular.

Downloaded By: [Carl Zeiss AG] At: 12:49 11 November 2009

Appendix A

In order to obtain the relation between the scattering angle θ and the goniometer angle θ_g we show in figure A 1 a sketch of the three-dimensional experiment with every relevant angle indicated. Note that, in comparison with figure 1, only the part above the plane of symmetry is drawn, which is indicated by the lightly shaded plane. The more darkly shaded plane is a projection of a part of one scattering experiment on this plane of symmetry.

The relation between θ and θ_g can be found by applying Pythagoras' theorem

$$\overline{OB}^2 + \overline{AB}^2 = \overline{OA}^2 \tag{A1}$$

and noting that

$$\cos\left(\frac{\theta_g}{2}\right) = \frac{\overline{OB}}{\overline{OD}}, \cos\left(\frac{\delta_{3D}}{2}\right) = \frac{\overline{OD}}{\overline{OC}}, \cos\left(\frac{\theta}{2}\right) = \frac{\overline{OA}}{\overline{OC}}. \tag{A2}$$

The height of the detector or the laser is invariant upon changing the goniometer angle, that is

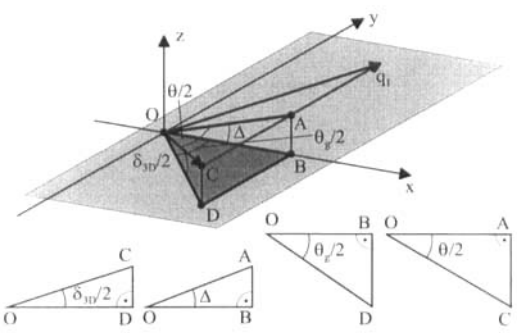

Figure A 1. Scheme of the three-dimensional set-up with all relevant angles indicated. The triangles used for the calculation are drawn separately.

$$\overline{AB} = \overline{CD} = \overline{OC} \sin\left(\frac{\delta_{3D}}{2}\right). \tag{A 3}$$

Combination yields the desired result:

$$\cos\left(\frac{\theta}{2}\right) = \left[\cos^2\left(\frac{\delta_{3D}}{2}\right)\cos^2\left(\frac{\theta_g}{2}\right) + \sin^2\left(\frac{\delta_{3D}}{2}\right)\right]^{1/2}. \tag{A 4}$$

Accordingly, the tilt angle Δ can be found easily:

$$\sin \Delta = \frac{\overline{AB}}{\overline{OA}} = \frac{\sin(\delta_{3D}/2)}{\cos(\theta/2)} \tag{A 5}$$

Equations (A 4) and (A 5) are shown in figure 4 after inversion.

As the polarization of the incident light remains fixed and perpendicular to the plane of symmetry (V), a tilting of the scattering plane is equivalent to introducing a component H, the magnitude of which increases with increasing tilt angle. If there were no analyser, the corresponding measured scattered intensity would be

$$\frac{I_{VU}}{I_0} = \cos^2 \Delta' + \sin^2 \Delta' \cos^2 \theta, \tag{A 6}$$

with $\Delta' = \Delta - \delta_{3D}/2$. This setting is equivalent to regarding the orientation of the polarization components before and behind the focusing lenses without the complication of the difference angle. If there is an analyser present, which is also kept fixed with respect to the plane of symmetry, we can, as usual, calculate the measured intensity for a V_V (polarized) or a V_H (depolarized) experiment. We obtain

$$\begin{aligned} \frac{I_{VV}}{I_0} &= \cos^2 \Delta'' \cos^2 \Delta' + \sin^2 \Delta'' \sin^2 \Delta' \cos^2 \theta, \\ \frac{I_{VH}}{I_0} &= \sin^2 \Delta'' \cos^2 \Delta' + \cos^2 \Delta'' \sin^2 \Delta' \cos^2 \theta, \end{aligned} \tag{A 7}$$

with $\tan \Delta'' = \cos \theta \tan \Delta'$. This equation can be understood as follows. As the incident polarization can be decomposed into its components V and H, we obtain $\tan \Delta' = H/V$. For the scattered field, however, the polarization component H depends on θ, leading to $\tan \Delta'' = (H \cos \theta)/V = \tan \Delta' \cos \theta$. Again, the corresponding component has to be taken into account for the scattered light, which leads to equation (A 7). Note that one obtains, as expected, $I_{VU}/I_0 = (I_{VV} + I_{VH})/I_0$, which still depends on θ, in contrast with a two-dimensional set-up, where no H component is present in the incident light ($\Delta' = 0°$). Note in addition that, beyond the scattering angle where $I_{VV} = I_{VH}$, the dominant component of the incident light with respect to the scattering plane is H instead of V.

Appendix B

Using rectangular cuvettes, the scattered intensities have to be corrected for Fresnel refraction and turbidity. We assume that the polarization of the incident light is parallel to the cuvette's surface and that the surface normal lies in the refraction plane, that is we ignore the small effects due to the angle δ_{3D}. The

Downloaded By: [Carl Zeiss AG] At: 12:49 11 November 2009

Fresnel formulae yield for the transmitted light $T = I/I_0$ through a single glass surface (subscript G), embedded in water (subscript W) on both sides:

$$T_{WG} = \frac{n_G \cos\theta_G}{n_W \cos\theta_W} \frac{4 \sin^2\theta_G \cos^2\theta_W}{\sin^2(\theta_W + \theta_G)},$$
$$T_{GW} = \frac{n_W \cos\theta_W}{n_G \cos\theta_G} \frac{4 \sin^2\theta_W \cos^2\theta_G}{\sin^2(\theta_G + \theta_W)}. \tag{B 1}$$

For a rectangular cuvette with two parallel surfaces this gives

$$T = T_{WG}^2 T_{GW}^2 = \frac{256 \sin^4\theta_G \cos^4\theta_W \sin^4\theta_W \cos^4\theta_G}{\sin^8(\theta_G + \theta_W)}, \tag{B 2}$$

where $\theta_W \equiv \zeta$. With $\lambda = 790\,\text{nm}$, we have $(\sin\theta_G)/(\sin\theta_W) = n_W/n_G = 1.329/1.516$ (UK50).

If the turbidity of the sample is not negligible, an angle-dependent correction has to be added, which can be calculated easily to be

$$T(\zeta) = \exp[-l(\zeta)\tau] = \exp\left(-d\frac{\tau}{\cos\zeta}\right), \tag{B 3}$$

where d is the thickness of the cuvette, $l(\zeta)$ is the light path through the cuvette and $\tau = d^{-1} \ln(I_0/I)$ is the turbidity of the sample.

Equations (B 2) and (B 3) have been used in order to draw the theoretical curves in figure 8.

Downloaded By: [Carl Zeiss AG] At: 12:49 11 November 2009

References

[1] Berne, B. J., and Pecora, R., 1976, *Dynamic Light Scattering* (New York: Wiley); Chu, B., 1991, *Laser Light Scattering* (Boston; Massachusetts: Academic Press).
[2] Phillies, G. D. J., 1981, *J. chem. Phys.*, **74,** 260.
[3] Phillies, G. D. J., 1981, *Phys. Rev.* A, **24,** 1939.
[4] Schätzel, K., 1991, *J. mod. Optics*, **38,** 1849.
[5] Pine, D. J.,Weitz, D. A., Chaikin, P. M., and Herbolzheimer, E., 1988, *Phys. Rev. Lett.*, **60,** 1134; Maret, G., and Wolf, P. E., 1987, *Z. Phys.* B, **65,** 409.
[6] Segrè, P. N., van Megen, W., Pusey, P. N., Schätzel, K., and Peters, W., 1995, *J. mod. Optics*, **42,** 1929.
[7] Arecchi, F. T., Corti, M., Degiorgio, V., and Donati, S., 1971, *Optics Commun.*, **3,** 284.
[8] Burstyn, H. C., and Sengers, J. V., 1983, *Phys. Rev.* A, **27,** 1071.
[9] Dhont, J. K. G., and de Krui, C. G., 1983, *J chem. Phys.*, **79,** 1658.
[10] Mos, H. J., Pathmamanoharan, C., Dhont, J. K. G., and de Kruif, C. G., 1986, *J. chem. Phys.*, **84,** 45.
[11] Drewel, M., Ahrens, J., and Podschus, U., 1989, *J. opt. Soc. Am.*, **7,** 206.
[12] Segrè, P. N., Meeker, S. P., Pusey, P. N., and Poon, W. C. K., 1995, *Phys. Rev. Lett.*, **75,** 958.
[13] Overbeck, E., Sinn, C., Palberg, T., and Schätzel, K., 1997, *Colloids Surf.* A, **122,** 83.
[14] Overbeck, E., Sinn, C., and Palberg, T., 1997, *Prog. Colloid Interface Sci.*, **104,** 117.
[15] Urban, C., and Schurtenberger, P., 1998, *Prog. Colloid Interface Sci.*, **110,** 61.
[16] Aberle, L. B., Wiegand, S., Schröer, W., and Staude, W., 1997, *Prog. Colloid Interface Sci.*, **104,** 121.

[17] SINN, C., NIEHÜSER, R., OVERBECK, E., and PALBERG, T., 1998, *Prog. Colloid Interface Sci.*, **110,** 8.
[18] URBAN, C., and SCHURTENBERGER, P., 1998, *J. Colloid Interface Sci.*
[19] RIČKA, J., 1993, *Appl. Optics*, **32,** 2860.
[20] FLAMMER, I., and RIČKA, J., 1997, *Appl. Optics*, **36,** 7508.
[21] OVERBECK, E., SINN, C., FLAMMER, I., and RIČKA, J., 1998, *Rev. scient. Instrum.*, **69,** 3515.
[22] WIEMAN, C. E., and HOLBERG, L., 1991, *Rev. scient. Instrum.*, **62,** 1.
[23] FELDERHOF, B. U., 1978, *J. Phys.* A, **11,** 929.

Downloaded By: [Carl Zeiss AG] At: 12:49 11 November 2009